



Reducing ROS generation and accelerating the photocatalytic degradation rate of PPCPs at neutral pH by doping Fe-N-C to g-C₃N₄

Hankun Yang^a, Wenyu Wang^{a,b}, Xue Wu^a, Muhammad Saboor Siddique^{a,c}, Zhaoyang Su^d, Mengjie Liu^a, Wenzheng Yu^{a,*}

^a State Key Laboratory of Environmental Aquatic Chemistry, Key Laboratory of Drinking Water Science and Technology, Research Center for Eco-Environmental Sciences, Chinese Academy of Sciences, Beijing 100085, People's Republic of China

^b State Key Laboratory of Separation Membrane and Membrane Processes, School of Environmental Science and Engineering, Tianjin University, Tianjin 300387, People's Republic of China

^c University of Chinese Academy of Sciences, Beijing 100049, People's Republic of China

^d Center for the Environmental Implications of Nanotechnology, Duke University, Durham, NC 27708, United States



ARTICLE INFO

Keywords:
Fe-N-C
g-C₃N₄
ROS
Photocatalysis
PPCPs

ABSTRACT

In this study, we designed and synthesized a 1% Fe-N-C nanotube (FeCNT) doped g-C₃N₄ (1%FeCNT@C₃N₄) to reduce the biotoxicity of g-C₃N₄ by reducing ROS generation and enhance its catalytic efficiency at the same time. The 1%FeCNT@C₃N₄ can not only effectively reduce the ROS generation at neutral pH but also had an extremely low electron-hole pairs recombination rate, which was attributed to the fact that O₂ undergone a four-electron oxygen reduction reaction (ORR) pathway at the Fe-N-C site. Additionally, the degradation results of tetracycline hydrochloride (TH) and Naproxen (NPX) by 1%FeCNT@C₃N₄ and g-C₃N₄ showed that the reaction rate constants of 1%FeCNT@C₃N₄ ($0.0176 \pm 0.0012 \text{ min}^{-1}$ and $0.05045 \pm 0.0010 \text{ min}^{-1}$ for TH and NPX, respectively) were much higher than those of g-C₃N₄ ($0.0098 \pm 0.0004 \text{ min}^{-1}$ and $0.0281 \pm 0.0008 \text{ min}^{-1}$ for TH and NPX, respectively). Moreover, the 1%FeCNT@C₃N₄ is proved to retain its high catalysis property in surface water.

1. Introduction

Pharmaceutical and Personal Care Products (PPCPs) are a kind of organic pollutants widely existing in various water bodies with a great threat to the environment and human health [1–3]. Most of the PPCPs have a molecular weight within the limit of 1 kDa and their concentrations are extremely low in nature water, which makes them difficult to be removed [4]. The common methods for PPCPs removal/degradation include the advanced oxidation process (AOP), powder activated carbon (PAC)/other adsorbents adsorption, reverse osmosis/nanofiltration (RO/NF), UV light radiation, activated sludge process/artificial wetland, and photocatalytic degradation [5–8]. The above processes have a good removal effect on PPCPs. However, advantages and shortages are mutual.

Among the above-mentioned methods, photocatalysis is considered a low energy cost and environmentally friendly water treatment process. In the general photocatalytic degradation process, the organic pollutions are degraded by the photogenerated electron holes and/or reactive

oxygen species (ROS) which are from the photocatalyst. As known, ROS is the main product of most photocatalysts in reactions and has strong oxidation, and is toxic to organisms [9–12]. Many high effective photocatalysts are thought to have the potential for application in water treatment, such as Fe₂O₃, CoFe₂O₄, Ag₃PO₄, TiO₂, ZnO, SiC, and g-C₃N₄ [13–15]. However, almost all of these photocatalysts can generate a large number of hydroxyl radicals, which are toxic to aquatic organisms and may cause secondary damage to the environment [16].

To minimize the hazard of radicals to aquatic organisms, the generation of hydroxyl radicals and their migration to the ambient environment should be reduced nanoreactors can limit the reaction inside a nano-size volume, which effectively enhances the reaction efficiency by increasing the concentration of free radicals [17,18]. However, the core-shell catalyst has a cumbersome preparation process and a high cost, which may limit its application in industrial and environmental remediation. In contrast, limiting the generation of free radicals may be a low-cost, feasible, and effective solution to decrease the potential risks of free radicals. According to the general catalytic mechanism of

* Corresponding author.

E-mail address: wzyu@rcees.ac.cn (W. Yu).

photocatalysis, there are two useful methods to limit the generation of hydroxyl radicals, namely, changing the acceptor of photogenerated electrons or changing the product of the oxygen reduction reaction (ORR) process [13,19,20]. For changing the acceptor of photogenerated electrons, if there is no effective means of energy or material recovery, the energy of photogenerated electrons will be wasted. Therefore, to limit the generation of hydroxyl radicals, a complete reduction of O₂ to H₂O could be a better choice.

To achieve the goal of reducing ROS production and verify the above-mentioned mechanism, composite photocatalysts were selected to be used. The g-C₃N₄ and Fe-N-C were chosen as the subject and object materials, respectively. The g-C₃N₄ is a semiconductor with the advantage of absorbance in visible light range, low cost, high oxidation potential, and wide-bandgap, thus it was widely used as the subject material of composite catalysts [13,21]. Fe-N-C is one of the most efficient catalysts for ORR at the pH range of neutral to alkaline, which is better than the Pt nanoparticle catalyst and also has outstanding stable properties [22–24]. In this study, the Fe-N-C nanotube (FeCNT) was combined with g-C₃N₄ to act as the ORR function site of the composite material (FeCNT@g-C₃N₄) to avoid the generation of hydroxyl radical by completely reducing O₂ to H₂O. Two PPCPs, the tetracycline hydrochloride (TH) and Naproxen (NPX) were used as the model molecules to verify the catalytic property of the FeCNT@g-C₃N₄. After FeCNT@g-C₃N₄ was prepared, its morphology, structure, and composition were characterized, and two types of PPCPs were used to test the photocatalytic degradation rate of the PPCPs under different conditions. Then, the catalytic mechanism of FeCNT@g-C₃N₄ was studied. Finally, the photocatalytic degradation rates of TH and NPX in surface water were tested. The target of this study is that the generation of ROS in photocatalytic degradation of PPCPs by FeCNT@g-C₃N₄ was greatly lower than the un-doped g-C₃N₄, while it did not affect the degradation efficiency of the PPCPs by photocatalyst. This study aimed at finding a simple method to reduce the ROS generation of the photocatalysis catalyst and discussed the application potential of the FeCNT@g-C₃N₄ for environmental remediation.

2. Materials and methods

2.1. Preparation and characterizations of FeCNT@g-C₃N₄

The synthesis method of g-C₃N₄ was modified according to various synthesis methods in the previous studies [13,25]. Briefly, 10 g of melamine was put into an alumina combustion boat with a cover, then heated to 550 °C at a heating rate of 10 °C/min in a tube furnace, and maintained at 550 °C for 4 h. All experiments were performed under an N₂ atmosphere with a flow of 160 mL/min. The obtained yellow product was g-C₃N₄.

The preparation method of FeCNT was reported by Peng and Wang's team and was partially modified in this study [22]. The detail is as follow. Firstly, 3.0 g FeCl₃·6H₂O and 3.0 g melamine were dispersed uniformly in 100 mL ethanol by ultrasonic for 0.5 h, and then the mixture was heated under magnetic stirring at 110 °C until dry. Subsequently, the dried sample was heated to 500 °C at a rate of 10 °C/min, then heated to 800 °C at a rate of 5 °C/min, and maintained at 800 °C for 2 h. All of the heat processes were in a tube furnace under an N₂ atmosphere (with a flow of 160 mL/min). The as-prepared sample was dispersed in 50 mL H₂SO₄ solution (0.5 M) for 8 h at room temperature and repeated 3 times to remove the unstable iron species. After acid treatment, the sample was washed with distilled water to neutral pH and then was washed with absolute ethanol 2 times to remove the unstable organic molecules. The washed sample was dried under vacuum at 80 °C overnight, and then the FeCNT was obtained.

To synthesize FeCNT@g-C₃N₄, the g-C₃N₄ and FeCNT were ground and mixed in an agate mortar, and the ratios of FeCNT/g-C₃N₄ (w/w) were from 0% to 50%. Afterward, the mixed materials were heated in a tube furnace at 550 °C with a rate of 10 °C/min and maintained at this

temperature for 2 h, and the highly pure N₂ gas was used as the protection gas. Finally, after natural cooling, the dark yellow powder was denoted as X%FeCNT@g-C₃N₄ (X indicated the weight percentage of FeCNT in the mixed material).

The field emission scanning electron microscope (FESEM, SU8020, HITACHI, Japan) and high-resolution field emission transport electron microscope (HR-FETEM, Tecnai G2 F30, FEI, the USA) were used to characterize the morphology of the catalyst. The X-ray powder diffraction (XRD, X'Pert 3 Powder, PANalytical, Netherlands) patterns were used to estimate the chemical constitution and crystal structure of the catalyst with Cu-K α target, and the 2θ was between 5 and 90 °. The Fourier transform infrared spectra (FTIR) were captured by FTIR spectroscopy (Spectra II, PerkinElmer, USA, with diamond ATR accessory). X-ray photoelectron spectroscopy (XPS) spectra were detected by XPS specter (QUANTERA-II SXM, ULVAC-PHI, Japan). The electron paramagnetic resonance (EPR) spectrometer (A300, BRUKER, USA) was used to detect the electron spin resonance (ESR) spectra, and the 5, 5-dimethyl-1-pyrroline N-oxide (DMPO, D2362, TCI, Japan) was used as the radical capturer for hydroxyl radical (•OH) in water and for superoxide radical (•O₂⁻) in methanol. The 3,3,5,5-Tetramethyl-1-pyrroline N-oxide (TMPO, J&K, China) was used as the radical capturer for ¹O₂ detection. The UV-vis spectra of the organic matters were detected by the UV-vis analyzer (UV-2600, Shimadzu, Japan). The solid diffuse reflectance spectrum (DRS) was measured by the UV-vis analyzer (UV-3600, Shimadzu, Japan). The photoluminescence spectra (PLS) and photon quantum yield were detected and calculated by the time-resolved spectrophotometer (F900, Edinburgh, the UK). The pH and conductivity of the samples were detected by the pH meter (METTLER TOLEDO, Switzerland). The light for the reaction was generated by a simulated sunlight source with a xenon lamp (CEL-PE300E-3A, 300 W, CEAulight, Beijing, China). Photoelectrochemical measurements were processed in a three-electrode system, 0.1 M Na₂SO₄ was used as the electrolyte solution; Pt wire electrode was used as the counter electrode, Ag/AgCl (0.20 V vs. NHE) electrode was used as the reference electrode, and FeCNT@g-C₃N₄/g-C₃N₄ modified indium-tin-oxide (ITO) glass was used as working electrodes, the binder was Nafion (5%, D-520, Alfa Aesar, USA); all of the electrochemical tests were detected by an electrochemical work station (CHI-660B, CHI, USA).

The concentration of H₂O₂ was detected by using Ti(SO₄)₂ method. In brief, Ti(SO₄)₂ was dissolved in H₂SO₄ solution (0.1 M) to prepare the indicator solution with a final concentration of 0.5 mg /mL. In the detection process, 1 mL sample, 1 mL H₂SO₄ solution (1 M), and 0.2 mL indicator solution were mixed and then detected the absorbance of the mixture was at 407 nm.

2.2. PPCPs degradation experiments

The default reaction condition in this study was maintained by dispersing 100 mg catalyst in 100 mL TH and NPX (J&K Scientific Ltd., Beijing) aqueous solution (20 mg/L and 10 mg/L, respectively) by ultrasonic, and then the solution was stirred in dark (300 r/min) for 30 min to balance the absorption before visible light irradiating.

The settings of the experiments, such as different pH, different atmosphere, and different NaSCN concentrations, were defaulted, and the reaction time was 60 min for the TH samples and 10 min for the NPX samples. For the experiments at different pH, the pH was adjusted to 3, 5, 7, 9, and 11 by adding 1 M HCl or 1 M NaOH solution; for the experiments in a different atmosphere, the N₂/O₂/air gases with a flow rate of 100 mL/min were applied 30 min before the reaction started and stopped after the reaction stopped; for the experiments with different NaSCN concentration, the concentration of NaSCN were set at 0, 1 and 10 mg/L, respectively. The cycling stability experiment was as same as the degradation experiment.

The reaction settings of the PPCPs in the surface water samples were as same as that of the degradation experiment in DI water. The basic data of surface water samples were shown in Table S1.

2.3. The method of PPCPs degradation rate analysis

The TH and NPX concentrations were measured by the UV-vis spectrophotometer at the wavelength of 357 nm and 230 nm, respectively. The remaining efficiency ($R\%$) of TH and NPX was defined as the function (1). t is the reaction time and C_t is the concentration at the reaction time t .

$$R\% = \frac{(C_0 - C_t)}{C_0} \quad (1)$$

3. Results and discussion

3.1. The characterization of FeCNT@C₃N₄

It can be seen that the size of the raw g-C₃N₄ was a micrometer scale, which was a distinct layered structure (Fig. S1a). The diameter of the FeCNT was about 80 nm with the complete tubular structure, and the iron core structure can be observed (Fig. S1b). The 1% FeCNT@C₃N₄ (Fig. 1a), which was after the second heat treatment of the FeCNT (1%, w/w%) and g-C₃N₄ mixture, it can be seen that the layered structure of g-C₃N₄ maintained, and FeCNT (20–80 nm width) and its sporadic fragments could be seen on the surface of g-C₃N₄. The HR-FETEM images showed that the wall of FeCNT has a layer structure, and there was no lattice fringe was observed in the g-C₃N₄ (Fig. 1b). In the 1% FeCNT@C₃N₄, the interface between the wall of FeCNT and g-C₃N₄ was clear, which indicated that the combination did not severely destroy the intrinsic structures of FeCNT and g-C₃N₄. In Fig. 1c, it can be seen that the Fe element is only distributed in the FeCNT region, which indicated the Fe element did not transport from FeCNT to g-C₃N₄ during the heat treatment. In the XRD spectra (Fig. 1d), it was seen that there were two strong and characteristic peaks belong to the (100) and (002) planes of g-C₃N₄ (13.1° and 27.5°, JCPDS No. 87–1526), and a group of peaks at 37.8, 43.9, 45.0, 46.0 and 49.2° belonged to the characteristic peaks of Fe-N-C (JCPDS No. 892867) [26–28]. The characteristic peaks of g-C₃N₄ and FeCNT both appeared in the spectra of the FeCNT@C₃N₄. It was also observed that with an increased dosage of doped FeCNT, the characteristic peaks of Fe-N-C became more obvious. There was a little decrease of the peak intensity that belongs to the (100) and (002) planes of g-C₃N₄ in the 1%- and 5%FeCNT@C₃N₄, but no difference between these two spectra, which can be attributed to the interlayer spacing changing of the g-C₃N₄ layer structure by the second heating (Fig. S1c) [25].

In the FTIR spectrum of FeCNT (Fig. S1d), characteristic peaks such as C≡C/C≡N, C=C/C=N were observed [24]. Similarly, the characteristic peaks of C=N, C-N stretching, and s-triazine ring system in g-C₃N₄ (1637, 1243, and 805 cm⁻¹) were also observed (Fig. 1e). With the doping dose of FeCNT increasing, it can be seen that the peak at 805 cm⁻¹ lightly decreased. Additionally, a slight increase of the series peaks (1100–1200 cm⁻¹) was also observed, which was attributed to the doping of FeCNT.

In the XPS spectra of C 1 s of g-C₃N₄ (Fig. 1f), the peak of C-C/C=C (284.6 eV), the peak of C-N (285.5 eV), and the peak of C=O (287.8 eV) can be observed [29,30]. Similarly, the N 1 s spectra of g-C₃N₄ (Fig. 1g), the peaks of N₁ (398.4 eV), N₂ (399.7 eV), N₃ (401.1 eV), and -C-N-H (404.5 eV) which belongs to π excitation of N were also observed [29, 31–33]. There was a new peak of O=C-O in carboxyl (288.6 eV) that appeared in the C 1 s spectrum of 1%FeCNT@C₃N₄ along with the increase of C-C/C=C (284.6 eV) peak area (Fig. 1h). In the N 1 s spectrum of 1%FeCNT@C₃N₄ (Fig. 1i), with the increase of N₂ and N₃ peaks, a new peak of N-Fe (399.2 eV) was also observed [24]. In contrast with the XPS spectra of FeCNT (Figs. S1e and S1f), the increase of C-C/C=C was found during the second heat treatment, which indicated that the g-C₃N₄ and FeCNT may mainly be combined through the C-C/C=C bonds. It also can observe the increase of the C-N bond which may be indicated that a small number of C-N bonds are also formed between g-C₃N₄ and

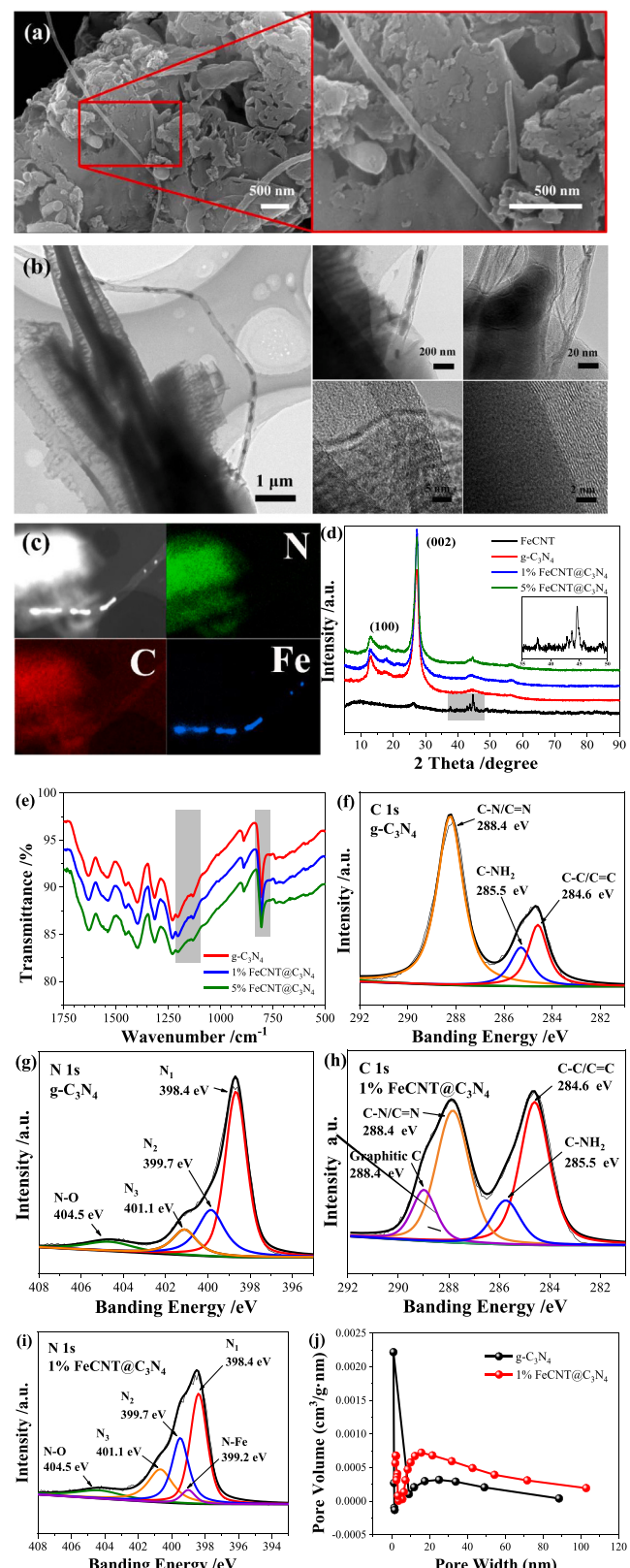


Fig. 1. FESEM images of g-C₃N₄ (a) and 1%FeCNT@C₃N₄ (b); the scale bar is 500 nm. XRD spectra (c), element distribution mapping (the scale bar is 1 μ m) (d), and FTIR spectra (e) of g-C₃N₄, 1%FeCNT@C₃N₄ and 5%FeCNT@C₃N₄. XPS spectra of C1s (f) and N1s (g) of g-C₃N₄, and C1s (h), N1s (i) of 1%FeCNT@C₃N₄. Pore width distribution of g-C₃N₄ and 1%FeCNT@C₃N₄ (j).

FeCNT.

Finally, the BET surface area and BJH pore size distribution were examined. There are many studies of CNT-doped materials that showed the doping of CNT will greatly change the BET surface area, but the improvement of catalytic performance and the changes of specific surface area are not directly related [34–36]. In this work, the BET surface area of 1%FeCNT@C₃N₄ was higher than that of g-C₃N₄ and 0%FeCNT@C₃N₄ (12.70, 6.69, and 6.70 m²/g, respectively), and the pore size distribution of g-C₃N₄ changed after CNT doping. The BJH pore size distribution showed that the mesopore (2–50 nm) volume of 1%FeCNT@C₃N₄ was significantly greater than that of g-C₃N₄, while the micropore volume (< 2 nm) of 1%FeCNT@C₃N₄ was less than that of g-C₃N₄ (Fig. 1j). The N₂ adsorption-desorption isotherms of 1%FeCNT@C₃N₄ and g-C₃N₄ were shown in Fig. S1g.

According to the above data, it was believed that there were some heterojunctions formed, which were the formed C-C/C=C or C-N bonds between g-C₃N₄ and FeCNT. And the new bonds, or the heterojunctions, only distribute on the surface of g-C₃N₄. The Fe-N-C sites are distributed on the N-doped carbon nanotubes (CNT) in a dot shape, thus, the structure of FeCNT@C₃N₄ was more like the fuel cell composed of the cathode (Fe-N-C), anode (g-C₃N₄), and was connected by wires (N-doped CNT). The possible synthesis and covalent bond formation processes of 1%FeCNT@C₃N₄ were shown in Scheme 1.

3.2. The photocatalytic performance of FeCNT@C₃N₄ for PPCPs degradation

To compare the photocatalytic activities of FeCNT@C₃N₄ and g-C₃N₄, a series of photocatalytic degradation experiments were performed using TH and NPX as the model PPCPs under visible light irradiation. It was found that the 1%FeCNT@C₃N₄ had the highest photocatalytic degradation efficiency for both TH and NPX in all of the FeCNT@C₃N₄ catalysts; thus, it was used for the subsequent catalyst testing (Figs. S2). Fig. S2 showed that the adsorption amount of the 1%FeCNT@C₃N₄ for TH and NPX was not significantly different from that of the g-C₃N₄ and 0%FeCNT@C₃N₄ for these two PPCPs.

From Fig. 2a, it was found that after 120 min of light irradiation, about 65% and 80% of TH was degraded by g-C₃N₄ and 1%FeCNT@C₃N₄, respectively. Similarly, in Figs. 2b, 1%FeCNT@C₃N₄ exhibited a remarkable photocatalytic degradation efficiency, with more than 70% of NPX degraded in less than 20 min, while the g-C₃N₄ required at least 60 min to achieve the same effect. In Fig. 2c, the

catalytic reaction constant of TH photocatalytic degradation by g-C₃N₄ was calculated according to the pseudo-first-order kinetics reaction, and the catalytic reaction constant of TH was $0.0098 \pm 0.0004 \text{ min}^{-1}$ by function (2) [37,38]. Using the same method, it can be calculated that the reaction rate constant of TH degradation under the photocatalysis of 1%FeCNT@C₃N₄ was $0.0174 \pm 0.0012 \text{ min}^{-1}$, which was nearly double times higher than that of g-C₃N₄, indicating that 1%FeCNT@C₃N₄ had higher catalytic efficiency than g-C₃N₄. In Fig. 2d, it can be calculated that the catalytic reaction constant of g-C₃N₄ and 1%FeCNT@C₃N₄ for NPX photocatalytic degradation were $0.0281 \pm 0.0008 \text{ min}^{-1}$ and $0.05045 \pm 0.0010 \text{ min}^{-1}$, respectively.

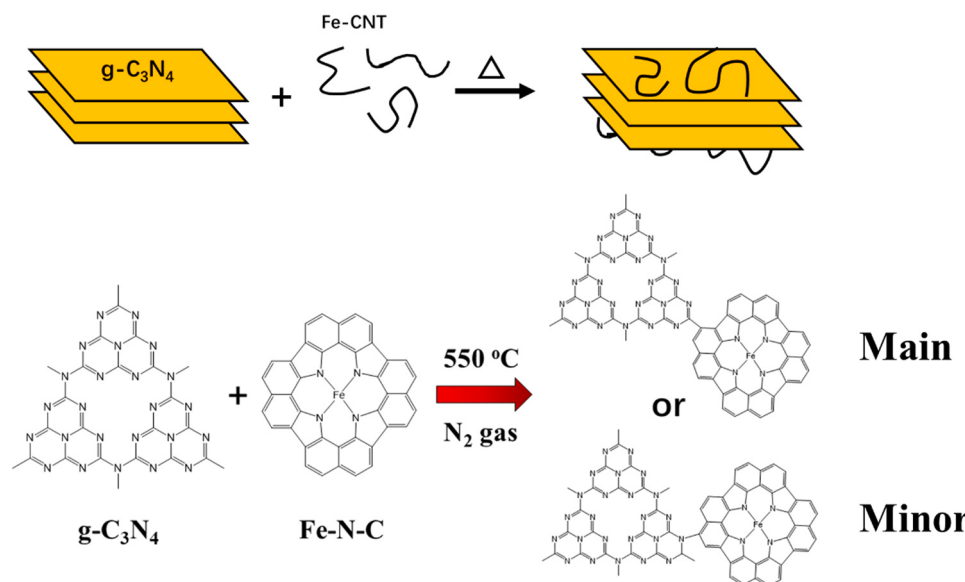
$$k = -\ln\left(\frac{C_t}{C_0}\right)/t \quad (2)$$

The effects of pH on the photocatalytic degradation efficiency by 1%FeCNT@C₃N₄ and g-C₃N₄ for TH and NPX were observed at the pH of 3, 5, 7, 9, and 11, respectively. In Fig. 2e, the results showed that the photocatalytic efficiency of 1%FeCNT@C₃N₄ is much higher than that of g-C₃N₄ in both acidic and alkaline conditions, but has a slight decrease at pH 7. In Fig. 2f, the pH increase had barely any effect on the photocatalytic degradation efficiency of NPX under the catalysis of the 1%FeCNT@C₃N₄ but had a seriously negative effect on the g-C₃N₄, which was different from the trend of TH. The mechanism will be discussed in the next section.

Finally, a cyclic photocatalytic experiment for TH and NPX was conducted to determine the stability of 1%FeCNT@C₃N₄ (Figs. 2g and 2h). It can be seen that there was no significant change in the catalytic efficiency after four cycles in TH or NPX degradation, indicating that 1%FeCNT@C₃N₄ had remarkable stability for PPCPs degradation.

3.3. The photocatalytic mechanism of FeCNT@C₃N₄

There are already a lot of researches on the general photocatalytic mechanism of g-C₃N₄ in PPCPs degradation: in simple terms, the photogenerated electrons and holes are generated after g-C₃N₄ had been illuminated, and O₂ molecules act as the photoelectron acceptor which was reduced to hydroxyl radical or hydrogen peroxide to subsequently oxidize the PPCPs. Meanwhile, the generated electron-hole pairs can also oxidize the PPCPs [13]. This kind of catalytic mechanism seems to have a high reaction efficiency. However, due to the slow reaction rate of O₂ on the surface of g-C₃N₄, the photogenerated electrons and hole pairs generated via illumination have a high recombination rate, and



Scheme 1. The schematic formation process of FeCNT@C₃N₄.

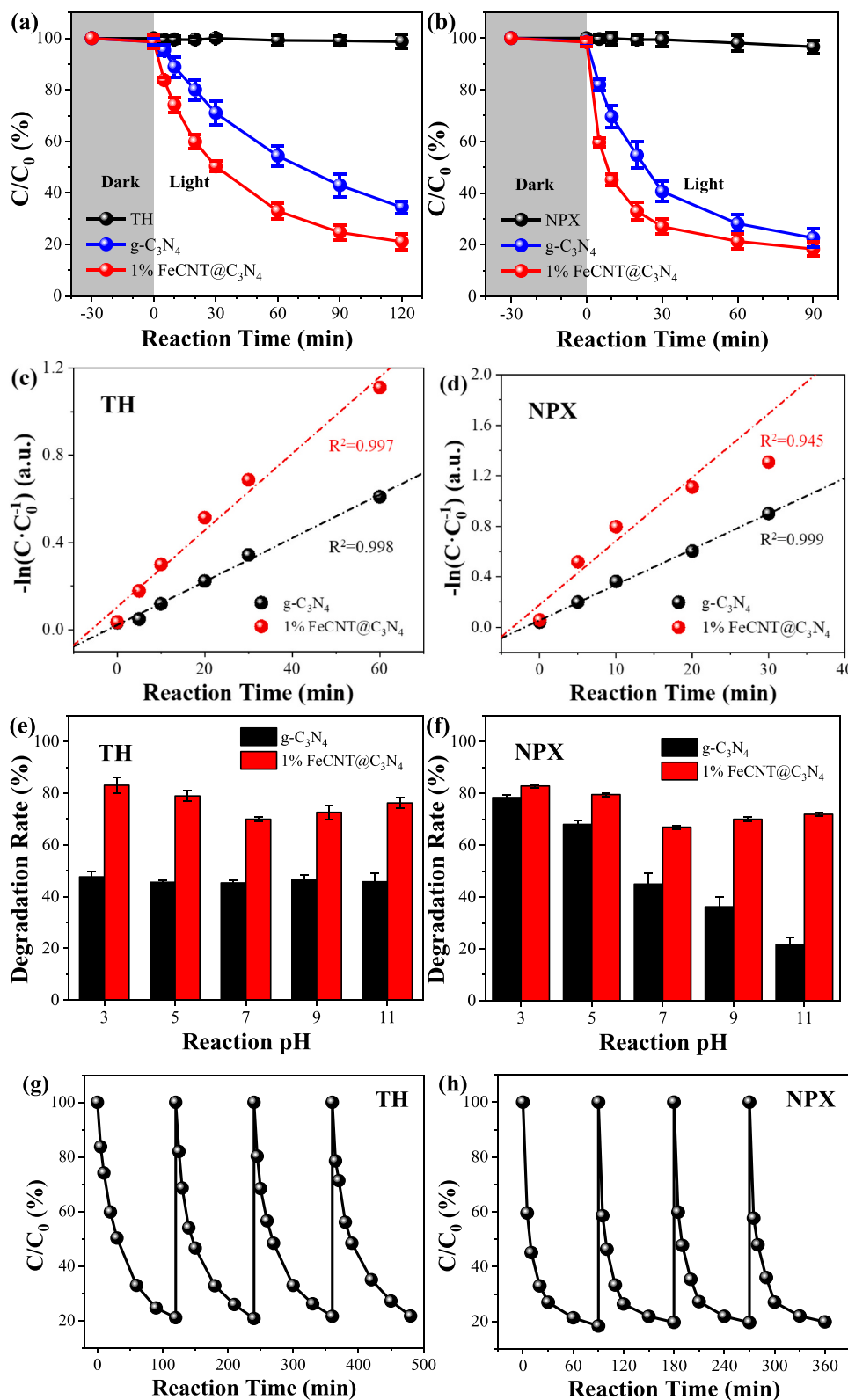
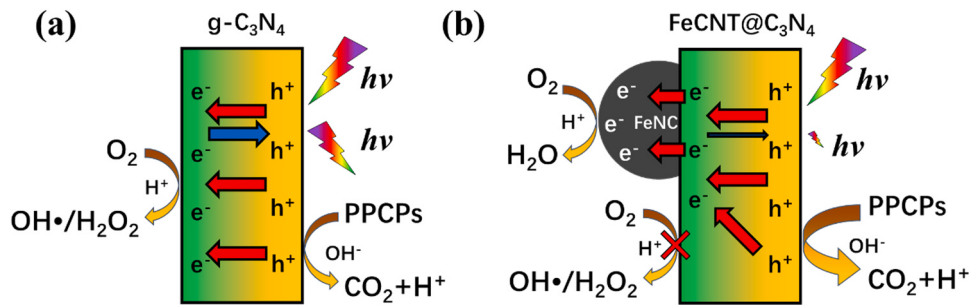


Fig. 2. Concentration changes of TH (a) and NPX (b) without catalyst, with $g\text{-C}_3\text{N}_4$ and $1\% \text{FeCNT}@C_3N_4$. Photocatalytic degradation reaction kinetics of TH (c) and NPX (d) over $g\text{-C}_3\text{N}_4$ and $1\% \text{FeCNT}@C_3N_4$. The effect of pH on the TH (e) and NPX (f) under the $g\text{-C}_3\text{N}_4$ and $1\% \text{FeCNT}@C_3N_4$ catalysis; and the cycling stability of $1\% \text{FeCNT}@C_3N_4$ for the catalysis of TH (g) and NPX (h). The reaction conditions of (a)-(d) and (g)-(h) were default condition. The reaction time (e) - (f) was 60 min for TH samples and 20 min for NPX samples.

this high recombination rate greatly reduces the actual photocatalytic efficiency and energy efficiency (Scheme 2a) [39]. Additionally, the $g\text{-C}_3\text{N}_4$ is difficult to be directly applied for the highly toxic risk of its generated ROS (mainly super oxygen radicals and hydroxyl radicals), especially in environmental remediation and recovery.

To reduce the risk of ROS, a material designation and catalytic

mechanism were proposed and shown in Scheme 2b. Since the new and unique heterojunction was formed between FeCNT and $g\text{-C}_3\text{N}_4$, therefore, this structure can be compared with the cathode and anode of a fuel cell. The ORR occurs at the Fe-N-C site, while the oxidation reaction of organics occurs at electron holes on the surface of $g\text{-C}_3\text{N}_4$. The electrons pass through from $g\text{-C}_3\text{N}_4$ to Fe-N-C sites by the carbon structure in



Scheme 2. The electron transportation and reaction schematic diagram of g-C₃N₄ (a) and FeCNT@C₃N₄ (b).

FeCNT. It is shown that it is an effective method to improve the stability of electron-hole to derive the photogenerated electrons from the semiconductor structure by forming heterojunction [40,41]. The Fe-N-C on the surface of FeCNT@C₃N₄ can serve as the ORR active sites, which will effectively improve the ORR reaction efficiency by decreasing the recombination rate of photogenerated electron-hole pairs, and suppress the generation of ROS to reduce the biotoxicity of photocatalysts.

To verify the above mechanism, the PLS and photon yield of the g-C₃N₄ and 1%FeCNT@C₃N₄ were examined. According to the mechanism of photoluminescence generation, the higher the photon quantum yield, the stronger the fluorescence intensity of photoluminescence, which indicates that the recombination rate of photogenerated electrons and holes is higher. It can be seen from Fig. 3a, the fluorescence peaks of g-C₃N₄ and 1%FeCNT@C₃N₄ were both at approximately 460 nm, but the fluorescence peak of 1%FeCNT@C₃N₄ is much lower than that of g-C₃N₄. Meanwhile, the calculated results of photon quantum yield showed that the photon quantum yield of 1%FeCNT@C₃N₄ and g-C₃N₄ was 0.13% and 1.84%, respectively (Fig. 3b). The PLS spectra and photon quantum yield calculations result indeed showed that the doped FeCNT can effectively reduce the recombination rate of photogenerated electron-hole pairs of g-C₃N₄, which lead to the improvement of energy efficiency [42].

It is believed that the photocatalytic degradation in aqueous solution generally requires dissolved O₂ (DO) as an electron acceptor to obtain free photoelectrons produced by the g-C₃N₄, and thus the photocatalytic degradation efficiency under different DO concentration were tested (Fig. 3c and 3d). It was seen that the low DO concentration extremely limited the photocatalytic degradation efficiency of g-C₃N₄ and 1% FeCNT@C₃N₄ in the degradation of TH and NPX to a low level; meanwhile, it was observed that after applying O₂ until saturation, the photocatalytic degradation efficiency of the samples was slightly improved compared with the reaction exposed to air. The above-mentioned results indicated that 1%FeCNT@C₃N₄ needed sufficient DO in the photocatalytic degradation processes as same as g-C₃N₄ but worked more efficiently.

Furthermore, the SCN⁻ ions were used to verify whether the Fe-N-C site acting as the oxygen reduction site for the photocatalytic degradation processes. SCN⁻ ions can combine with the Fe-N-C sites effectively and tightly, thereby blocking the ORR processes. In Fig. 3e, it was found that in the TH photocatalytic degradation reaction, the SCN⁻ did not affect the photocatalytic degradation efficiency of g-C₃N₄. However, with the SCN⁻ concentration increasing, the photocatalytic degradation efficiency of 1%FeCNT@C₃N₄ for TH decreased and finally reached the same degradation efficiency as g-C₃N₄. Besides, A similar result was observed in the photocatalytic degradation reaction NPX as shown in Fig. 3f.

The ESR detection was used to confirm that whether superoxide radicals or hydroxyl radicals appeared during the reaction. In Fig. 3g, it was seen that the 1%FeCNT@C₃N₄ produced little superoxide radicals; in Fig. 3h, it can be seen that the signal of hydroxyl radicals was extremely low. In contrast, g-C₃N₄ had the obvious signals of superoxide radical and hydroxyl radical under the same conditions. According to

the ORR processes, the superoxide radical transition state is the essential precursor for H₂O₂ generation [43,44]. The absence of superoxide radical indicated that only negligible hydrogen peroxide was produced by 1%FeCNT@C₃N₄ under the experimental conditions (Fig. S3a). And it was the same as the production of ¹O₂ (Fig. S3b). From the above, it was indicated that 1%FeCNT@C₃N₄ produced a negligible quantity of ROS during the photocatalytic process.

In Fig. 3i, the UV-vis DRS and the bandgap calculated results showed that the bandgap of the g-C₃N₄ was 2.70 eV which was 0.1 eV greater than that of the 1%FeCNT@C₃N₄. The conduction band (CB), valence band (VB) of g-C₃N₄, and 1%FeCNT@C₃N₄ were calculated based on the above DRS results and Mott-Schottky plots Fig. 3g. In Fig. 3k, it was found that the VB of 1%FeCNT@C₃N₄ was 1.55 eV, which was almost the same as the VB of g-C₃N₄ (1.56 eV). The CB of 1%FeCNT@C₃N₄ was -1.05 eV, which was higher than the CB of g-C₃N₄ (-1.16 eV). Meanwhile, Fe-N-C is an excellent catalyst for ORR that can greatly increase the reaction rate of oxygen reduction, and thereby effectively reduce the electron-hole pairs recombination rate of the 1% FeCNT@C₃N₄.

In the electrochemical impedance spectroscopy (EIS) Nyquist analysis, the radius of the arc is related to the electron transfer process at the liquid/solid interface. As shown in Fig. 3l, the EIS results indicated that the separation of photogenerated electron-hole pairs and interfacial electron transfer of the 1%FeCNT@C₃N₄ was significantly more effective and faster than that of the g-C₃N₄, which may be due to the quick electrons transfer guided by the FeCNT from g-C₃N₄ to electrode. These results showed that the doping of FeCNT was indeed conducive to reducing the electron-hole recombination rate and accelerating the electron transfer process [21,45]. In Fig. 3m, it can be seen that the periodic on/off photocurrents of 1%FeCNT@C₃N₄ were much higher than that of g-C₃N₄. This result is consistent with the EIS result.

The above data showed that the revealed photocatalytic degradation mechanism matched well with the theoretical mechanism of FeCNT@C₃N₄, which was mainly through the ORR processes on Fe-N-C to improve the catalytic efficiency by reducing the photogenerated electron-hole pairs recombination rate, and inhibited the generation of ROS. In the photocatalytic system without ROS generation, 1% FeCNT@C₃N₄ can only oxidize PPCPs through electron holes. To analyze this mechanism, the relevant adsorption experiments were carried out. In Fig. S4a, the adsorption amount of TH increased with the increase of the FeCNT doping amount. In Fig. S4b, the adsorption amount of NPX did not relate to the doping amount of FeCNT. These results indicated that the TH tended to adsorb on the surface of FeCNT, while NPX tended to adsorb on the surface of C₃N₄. According to Fig. S4c and S4d, it can be calculated that the saturated adsorption capacity (at 25 °C) of 1%FeCNT@C₃N₄ for TH and NPX was 0.4037 ± 0.0372 mg/g and 0.1411 ± 0.02876 mg/g, respectively. The saturated adsorption capacity (at 25 °C) of g-C₃N₄ for TH and NPX can be calculated as 0.0972 ± 0.0241 mg/g and 0.0634 ± 0.0137 mg/g, respectively (Fig. S4e and S4f). Although the adsorption amount of TH on 1% FeCNT@C₃N₄ was more than that of NPX, the degradation rate of TH was lower than that of NPX. This is because most of the TH was adsorbed on the surface of FeCNT which was far from the electron-hole and block

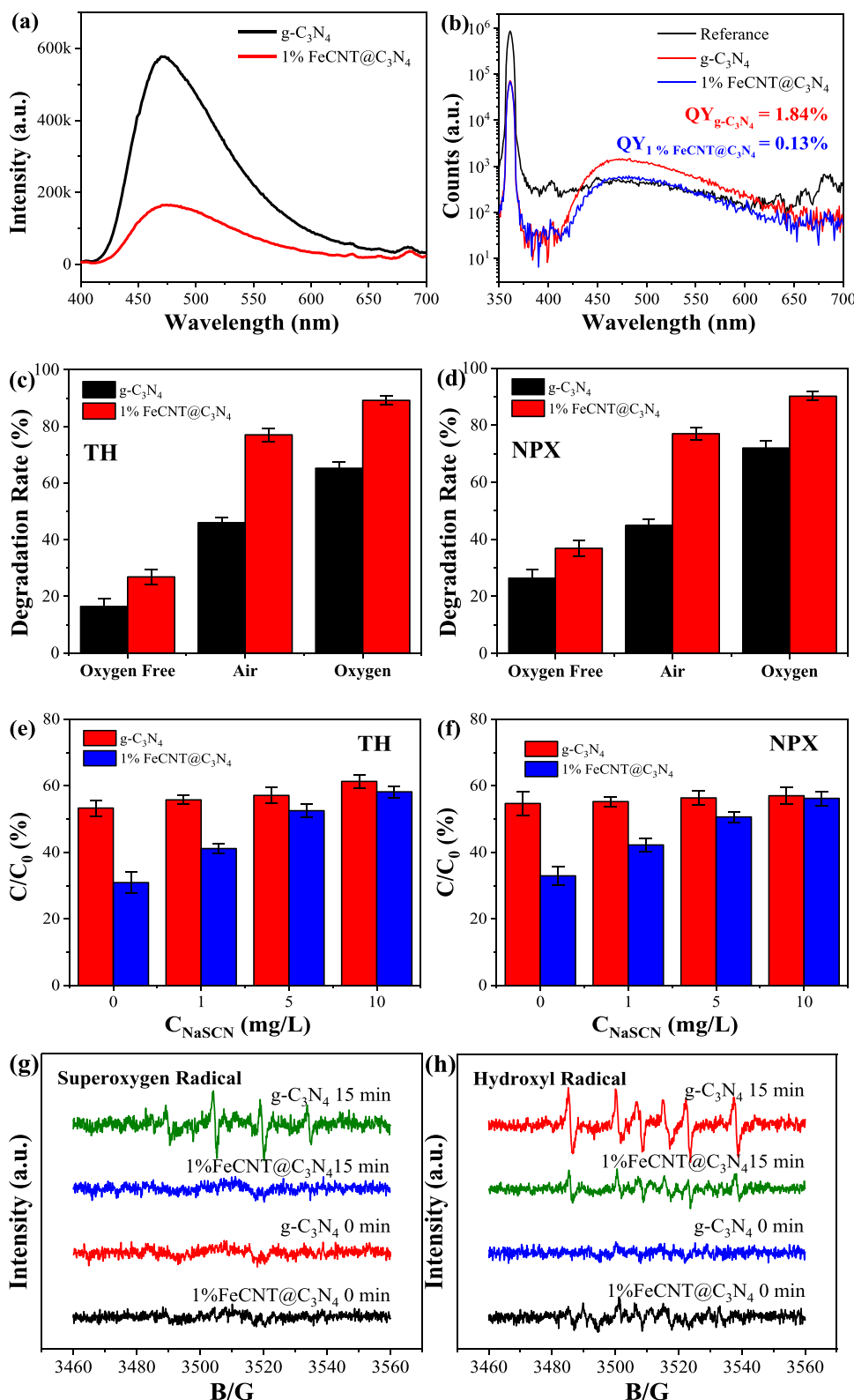


Fig. 3. Photoluminescence spectra (PLS) (a) and Photon quantum yield of $\text{g-C}_3\text{N}_4$ and 1% FeCNT@ C_3N_4 (b). The effect of O_2 on the TH (c) and NPX (d) under the $\text{g-C}_3\text{N}_4$ and 1% FeCN@ C_3N_4 catalysis. The effect of different concentrations of NaSCN on Fe-N-C site poisoning in TH (e) and NPX (f) degradation. ESR spectra of super oxygen radical (g) and hydroxyl radical (h) generated by $\text{g-C}_3\text{N}_4$ and 1%FeCNT@ C_3N_4 . UV-vis DRS and BG calculated results (i) and Mott-Schottky plots of $\text{g-C}_3\text{N}_4$ and 1% FeCNT@ C_3N_4 (j); Schematic illustration of band structures (CB: conduction band, VB: valence band) of FeCNT, $\text{g-C}_3\text{N}_4$, and 1%FeCNT@ C_3N_4 (k). EIS curves of $\text{g-C}_3\text{N}_4$ and 1%FeCNT@ C_3N_4 (l). Periodic on/off photocurrents of $\text{g-C}_3\text{N}_4$ and 1%FeCNT@ C_3N_4 (m); DMPO was used as the radical capturer for ESR measurement; PLS excited wavelength was 365 nm; the photocurrents were tested in 0.1 M Na_2SO_4 solution; the Mott-Schottky plots were detected at a fixed frequency of 800 Hz in 0.1 M Na_2SO_4 solution. The EIS was processed in 0.1 M KCl solution, the frequency was from 10^{-2} to 10^5 Hz.

the Fe-N-C sites to slow down the ORR processes. Herein, the effect of pH on the photocatalytic efficiency of TH and NPX can be explained according to the above mechanisms. First, the photocatalytic efficiency of TH and NPX on $\text{g-C}_3\text{N}_4$ is consistent with the effect of pH on its solubility [46,47]. It can be considered that TH had a weak adsorption capacity on the $\text{g-C}_3\text{N}_4$ surface, and therefore pH had little effect on the

photocatalytic efficiency almost not been affected by pH; while NPX has a strong adsorption capacity on $\text{g-C}_3\text{N}_4$, which made the photocatalytic efficiency easy to be affected by pH. While for the 1%FeCNT@ C_3N_4 , the change trends of photocatalytic efficiency were similar to that of the ORR with the change of pH, which can be considered that pH mainly affects the photocatalytic efficiency by affecting the ORR rate of 1%

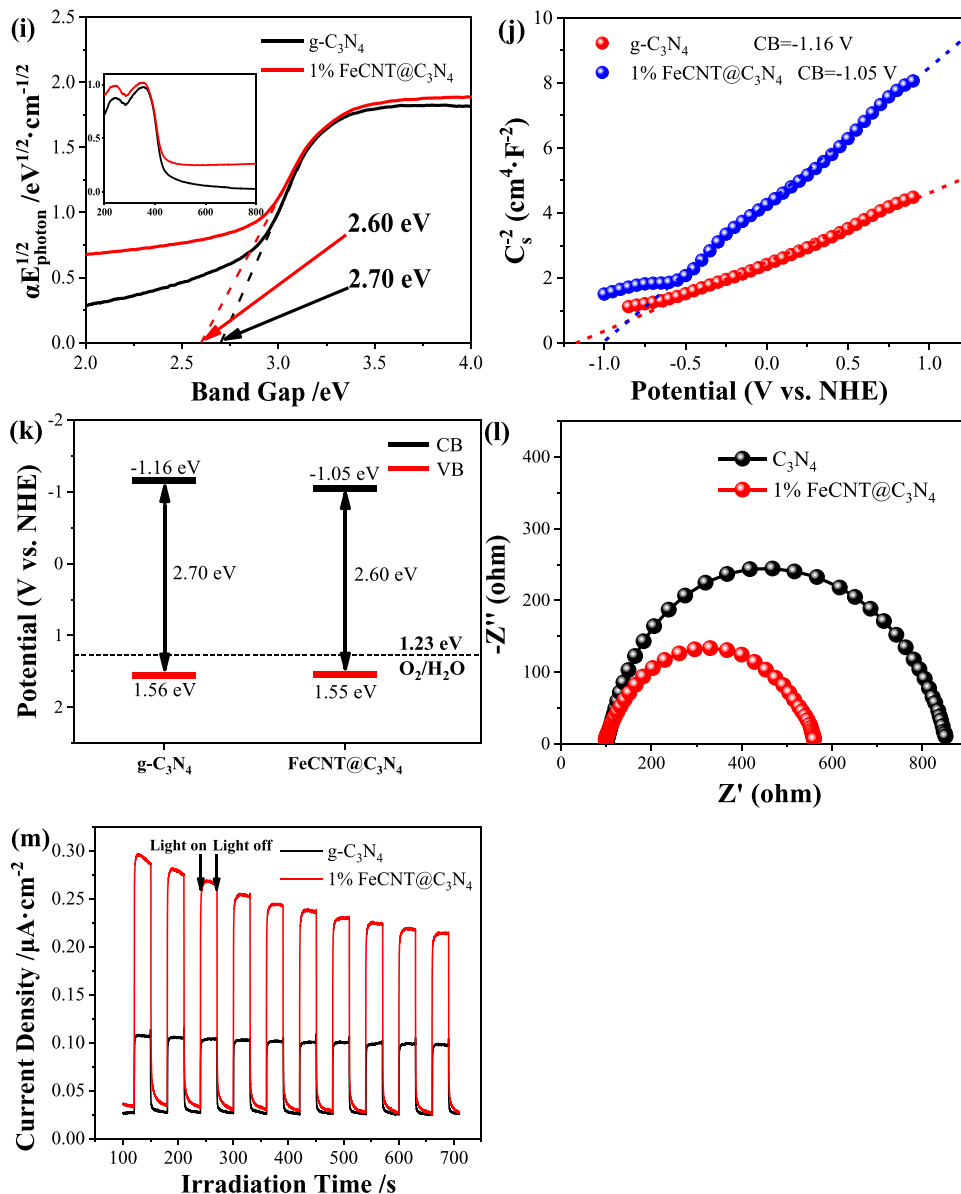


Fig. 3. (continued).

FeCNT@ $C_3\text{N}_4$ [48].

3.4. Application of FeCNT@ $C_3\text{N}_4$ in surface water

To verify the application of FeCNT@ $C_3\text{N}_4$ for PPCPs degradation in surface water, the filtered Qinghe river water (QH) and Olympic lake water (OL) were used to prepare the samples that contain 20 mg/L TH or 10 mg/L NPX and for the photocatalytic degradation test. As can be seen from Fig. 4a, the negative effect of OL on TH photocatalytic degradation by $g\text{-C}_3\text{N}_4$ was slightly higher (10% C/C₀ higher at 120 min) than that of QH. For NPX, the effect of surface water on photocatalytic efficiency was similar to that of TH. The results indicated that natural organic matter (NOM) in surface water had almost no effect on the photocatalytic efficiency of 1% FeCNT@ $C_3\text{N}_4$, which may be related to its adsorption characteristics on 1% FeCNT@ $C_3\text{N}_4$. However, the effect of NOM on the photocatalytic efficiency of $g\text{-C}_3\text{N}_4$ is slightly higher than that of 1% FeCNT@ $C_3\text{N}_4$, which was due to the oxidation of NOM by the ROS generated from $g\text{-C}_3\text{N}_4$ during the reaction [4,49]. Moreover, the catalytic efficiency of 1%FeCNT@ $C_3\text{N}_4$ on the PPCPs was not affected by NOM and was still much higher than that of $g\text{-C}_3\text{N}_4$ (Fig. 4c and 4d). Additionally, photodegradation of NOM was hardly catalyzed by the

FeCNT@ $C_3\text{N}_4$ (Fig. S5). The above results indicated that the 1% FeCNT@ $C_3\text{N}_4$ can selectively degrade the PPCPs in surface water with negligible affection by natural organic matters, which showed high application potential for the water treatment.

4. Conclusions

In this study, a new strategy was developed for $g\text{-C}_3\text{N}_4$ to effectively reduce the production of hydroxyl radicals and superoxide radicals in its photocatalysis process by doping Fe-N-C nanotubes (FeCNT@ $C_3\text{N}_4$). The mechanism is that the doped Fe-N-C reduces dissolved O₂ to H₂O by photo-generated electrons through the 4-electron pathway ORR. Furthermore, since the Fe-N-C also has the property of peroxidase nanozyme, and it did not produce the super-oxygen radical (as the precursors of H₂O₂), the H₂O₂ is also thought to be non-existent in the reaction. In short, this strategy can effectively reduce the generation of reactive oxygen species (ROS). Besides, the ORR by the doped Fe-N-C can effectively reduce the recombination rate of electron-hole pairs in $g\text{-C}_3\text{N}_4$, which can improve the efficiency of light illumination. It is found that the 1% (w/w) FeCNT doped $g\text{-C}_3\text{N}_4$ has the highest photocatalytic property. More importantly, although Fe-N-C doping

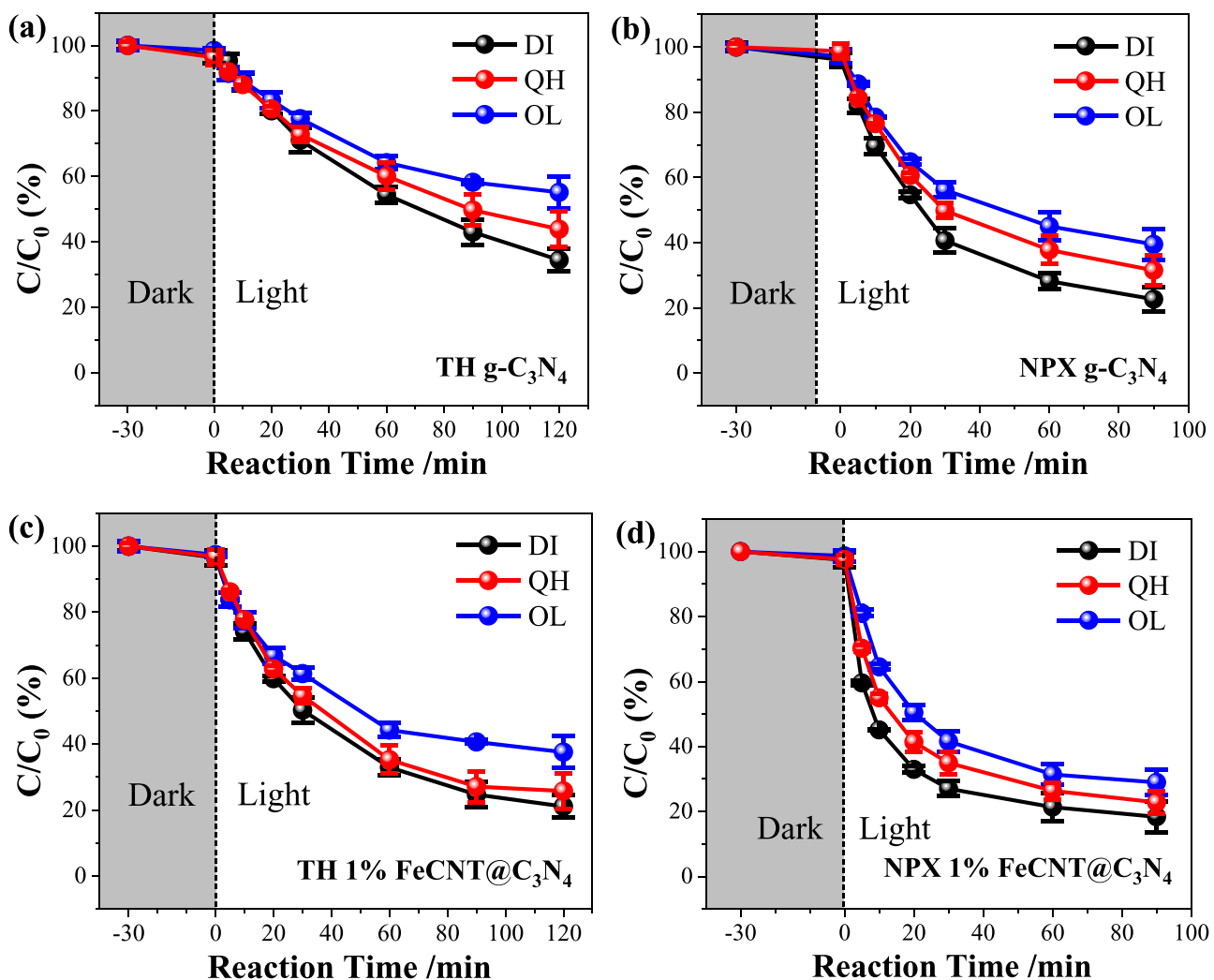


Fig. 4. Photocatalytic degradation experiments of TH (a) and NPX (b) in two types of surface water by $\text{g-C}_3\text{N}_4$. Photocatalytic degradation experiments of TH (c) and NPX (d) in two types of surface water by 1%FeCNT@ C_3N_4 . The pH of the surface water samples was adjusted to 7 by adding 0.1 M HCl solution. The reaction condition was the default condition.

effectively reduces ROS production, the degradation rate constant of TH and NPX under the photocatalysis of 1%FeCNT@ C_3N_4 ($0.0176 \pm 0.0012 \text{ min}^{-1}$ and $0.05045 \pm 0.0010 \text{ min}^{-1}$) is double higher than that of $\text{g-C}_3\text{N}_4$ ($0.0098 \pm 0.0004 \text{ min}^{-1}$ and $0.0281 \pm 0.0008 \text{ min}^{-1}$). Additionally, the NOM in surface water did not affect the catalytic efficiency of 1%FeCNT@ C_3N_4 . This manuscript provided an innovative strategy to reduce the ROS produced by photocatalytic nanomaterials and simultaneously improve the photocatalyst light efficiency. ROS is believed closely related to the aquatic toxicity of nanomaterials that are currently concerned, and thus, this study is of great significance for the application of photocatalytic nanomaterials in environmental remediation.

CRediT authorship contribution statement

Hankun Yang: Conceptualization, Methodology, Experiments design, Data analysis, Writing – original draft, editing, Supervision. **Wenyu Wang:** Conceptualization, Experiment design, Experiment execution, Data analysis. **Xue Wu:** Conceptualization, Experiments design, Writing – review & editing. **Muhammad Saboor Siddique:** Writing – review & editing. **Zhaoyang Su:** Writing – review & editing. **Mengjie Liu:** Writing – review & editing, Data analysis. **Wenzheng Yu:** Conceptualization, Experiments design, Experiments design, Data analysis, Writing – review & editing, Supervision, Project

administration, Resources.

Declaration of Competing Interest

The authors declare that they have no known competing financial interests or personal relationships that could have appeared to influence the work reported in this paper.

Acknowledgments

This work was supported by the National Natural Science Foundation of China (Grants 51108444), Key Research and Development Plan of the Ministry of Science and Technology (2019YFD1100104), China and Excellent Innovation Project of Research Center for Eco-Environmental Sciences, CAS (RCEES-EEI-2019-02), China.

Appendix A. Supporting information

Supplementary data associated with this article can be found in the online version at doi:10.1016/j.apcatb.2021.120790.

References

- [1] Z. Yao, W. Jiao, F. Shao, H. Song, H. Zhang, Q. Zhou, A. Li, Fabrication and characterization of amphiphilic magnetic water purification materials for efficient PPCPs removal, *Chem. Eng. J.* 360 (2019) 511–518.
- [2] A. Kumar, M. Khan, J. He, I.M.C. Lo, Visible-light-driven magnetically recyclable terephthalic acid functionalized g-C3N4/TiO₂ heterojunction nanophotocatalyst for enhanced degradation of PPCPs, *Appl. Catal. B: Environ.* 270 (2020), 118898.
- [3] S. Cheng, X. Zhang, X. Yang, C. Shang, W. Song, J. Fang, Y. Pan, The multiple role of bromide ion in PPCPs degradation under UV/chlorine treatment, *Environ. Sci. Technol.* 52 (2018) 1806–1816.
- [4] Y. Zhou, C. Chen, K. Guo, Z. Wu, L. Wang, Z. Hua, J.J.W.R. Fang, Kinetics and pathways of the degradation of PPCPs by carbonate radicals in advanced oxidation processes, *Water Res.* 185 (2020), 116231.
- [5] X. Yi, N.H. Tran, T. Yin, Y. He, K.Y. Gin, Removal of selected PPCPs, EDCs, and antibiotic resistance genes in landfill leachate by a full-scale constructed wetlands system, *Water Res.* 121 (2017) 46–60.
- [6] Y. Yang, Y.S. Ok, K.H. Kim, E.E. Kwon, Y.F. Tsang, Occurrences and removal of pharmaceuticals and personal care products (PPCPs) in drinking water and water/sewage treatment plants: a review, *Sci. Total Environ.* 596–597 (2017) 303–320.
- [7] J. Wang, S. Wang, Removal of pharmaceuticals and personal care products (PPCPs) from wastewater: a review, *J. Environ. Manag.* 182 (2016) 620–640.
- [8] E.L. Marron, W.A. Mitch, U.V. Gunten, D.L. Sedlak, A tale of two treatments: the multiple barrier approach to removing chemical contaminants during potable water reuse, *Acc. Chem. Res.* 52 (2019) 615–622.
- [9] Y. Nosaka, A.Y. Nosaka, Generation and detection of reactive oxygen species in photocatalysis, *Chem. Rev.* 117 (2017) 11302–11336.
- [10] P. Di Mascio, G.R. Martinez, S. Miyamoto, G.E. Ronsein, M.H.G. Medeiros, J. Cadet, Singlet molecular oxygen reactions with nucleic acids, lipids, and proteins, *Chem. Rev.* 119 (2019) 2043–2086.
- [11] C. Wang, Z. Yang, L.H. Tang, X.M. Wang, Q. Zhang, Potential risk and mechanism of microcystin induction by chiral metalaxyl, *Environ. Sci. Tech. Lett.* 5 (2018) 635–640.
- [12] Y. Guo, Y. Zhang, G. Yu, Y. Wang, Revisiting the role of reactive oxygen species for pollutant abatement during catalytic ozonation: The probe approach versus the scavenger approach, *Appl. Catal. B: Environ.* 280 (2021), 119418.
- [13] W.J. Ong, L.L. Tan, Y.H. Ng, S.T. Yong, S.P. Chai, Graphitic carbon nitride (g-C3N4)-based photocatalysts for artificial photosynthesis and environmental remediation: are we a step closer to achieving sustainability? *Chem. Rev.* 116 (2016) 7159–7329.
- [14] Z. Jiang, W. Wan, H. Li, S. Yuan, H. Zhao, P.K. Wong, A hierarchical Z-scheme alpha-Fe2O3/g-C3N4 hybrid for enhanced photocatalytic CO₂ reduction, *Adv. Mater.* 30 (2018), 1706108.
- [15] L. Jing, Y. Xu, S. Huang, M. Xie, M. He, H. Xu, H. Li, Q. Zhang, Novel magnetic CoFe2O4/Ag/Ag3VO4 composites: Highly efficient visible light photocatalytic and antibacterial activity, *Appl. Catal. B: Environ.* 199 (2016) 11–22.
- [16] I. Fenoglio, G. Greco, S. Livraghi, B. Fubini, Non-UV-induced radical reactions at the surface of TiO₂ nanoparticles that may trigger toxic responses, *Chem. Eur. J.* 15 (2009) 4614–4621.
- [17] B. Kwon, E. Han, W. Yang, W. Cho, W. Yoo, J. Hwang, B.-M. Kwon, D. Lee, Nano-Fenton reactors as a new class of oxidative stress amplifying anticancer therapeutic agents, *ACS Appl. Mater. Inter.* 8 (2016) 5887–5897.
- [18] T. Zeng, X. Zhang, S. Wang, H. Niu, Y. Cai, Spatial confinement of a Co3O4 catalyst in hollow metal-organic frameworks as a nanoreactor for improved degradation of organic pollutants, *Environ. Sci. Technol.* 49 (2015) 2350–2357.
- [19] W. Gu, L. Hu, J. Li, E. Wang, Hybrid of g-C3N4 assisted metal-organic frameworks and their derived high-efficiency oxygen reduction electrocatalyst in the whole pH range, *ACS Appl. Mater. Inter.* 8 (2016) 35281–35288.
- [20] H. Zhao, S. Chen, X. Quan, H. Yu, H. Zhao, Integration of microfiltration and visible-light-driven photocatalysis on g-C3N4 nanosheet/reduced graphene oxide membrane for enhanced water treatment, *Appl. Catal. B: Environ.* 194 (2016) 134–140.
- [21] Z. Lu, L. Zeng, W. Song, Z. Qin, D. Zeng, C. Xie, In situ synthesis of C-TiO₂/g-C3N4 heterojunction nanocomposite as highly visible light active photocatalyst originated from effective interfacial charge transfer, *Appl. Catal. B: Environ.* 202 (2017) 489–499.
- [22] G. Zhong, H. Wang, H. Yu, F. Peng, Nitrogen doped carbon nanotubes with encapsulated ferric carbide as excellent electrocatalyst for oxygen reduction reaction in acid and alkaline media, *J. Power Sources* 286 (2015) 495–503.
- [23] N. Cheng, J.C. Li, D. Liu, Y. Lin, D. Du, Single-atom nanozyme based on nanoengineered Fe-N-C catalyst with superior peroxidase-like activity for ultrasensitive bioassays, *Small* 15 (2019), 1901485.
- [24] M. Sun, D. Davenport, H. Liu, J. Qu, M. Elimelech, J. Li, Highly efficient and sustainable non-precious-metal Fe-N-C electrocatalysts for the oxygen reduction reaction, *J. Mater. Chem. A* 6 (2018) 2527–2539.
- [25] L. Liu, Y. Qi, J. Lu, S. Lin, W. An, Y. Liang, W. Cui, A stable Ag3PO4@g-C3N4 hybrid core@shell composite with enhanced visible light photocatalytic degradation, *Appl. Catal. B: Environ.* 183 (2016) 133–141.
- [26] Z. Zhu, H. Pan, M. Muruganathan, J. Gong, Y. Zhang, Visible light-driven photocatalytically active g-C3N4 material for enhanced generation of H₂O₂, *Appl. Catal. B: Environ.* 232 (2018) 19–25.
- [27] W. Yang, X. Liu, X. Yue, J. Jia, S. Guo, Bamboo-like carbon nanotube/Fe3C nanoparticle hybrids and their highly efficient catalysis for oxygen reduction, *J. Am. Chem. Soc.* 137 (2015) 1436–1439.
- [28] J. Ma, C. Wang, H. He, Enhanced photocatalytic oxidation of NO over g-C3N4-TiO₂ under UV and visible light, *Appl. Catal. B: Environ.* 184 (2016) 28–34.
- [29] R. You, H. Dou, L. Chen, S. Zheng, Y. Zhang, Graphitic carbon nitride with S and O codoping for enhanced visible light photocatalytic performance, *RSC Adv.* 7 (2017) 15842–15850.
- [30] J. Landoulsi, M.J. Genet, S. Fleith, Y. Touré, I. Liascukiene, C. Méthivier, P. G. Rouxhet, Organic adlayer on inorganic materials: XPS analysis selectivity to cope with adventitious contamination, *Appl. Surf. Sci.* 383 (2016) 71–83.
- [31] C. Li, Y. Du, D. Wang, S. Yin, W. Tu, Z. Chen, M. Kraft, G. Chen, R. Xu, Unique PCoN surface bonding states constructed on g-C3N4 nanosheets for drastically enhanced photocatalytic activity of H₂ evolution, *Adv. Funct. Mater.* 27 (2017), 1604328.
- [32] J. Li, D. Wu, J. Iocozzia, H. Du, X. Liu, Y. Yuan, W. Zhou, Z. Li, Z. Xue, Z. Lin, Achieving efficient incorporation of pi-electrons into graphitic carbon nitride for markedly improved hydrogen generation, *Angew. Chem. Int. Ed.* 58 (2019) 1985–1989.
- [33] K. Qi, W. Lv, I. Khan, S.-y Liu, Photocatalytic H₂ generation via CoP quantum-dot-modified g-C3N4 synthesized by electroless plating, *Chin. J. Catal.* 41 (2020) 114–121.
- [34] N.I. Andersen, A. Serov, P. Atanassov, Metal oxides/CNT nano-composite catalysts for oxygen reduction/oxygen evolution in alkaline media, *Appl. Catal. B: Environ.* 163 (2015) 623–627.
- [35] Z. Li, B. Gao, G.Z. Chen, R. Mokaya, S. Sotiropoulos, G. Li Puma, Carbon nanotube/titanium dioxide (CNT/TiO₂) core-shell nanocomposites with tailored shell thickness, CNT content and photocatalytic/photoelectrocatalytic properties, *Appl. Catal. B: Environ.* 110 (2011) 50–57.
- [36] N. Bouazza, M. Ouzzine, M.A. Lillo-Rodenas, D. Eder, A. Linares-Solano, TiO₂ nanotubes and CNT-TiO₂ hybrid materials for the photocatalytic oxidation of propene at low concentration, *Appl. Catal. B: Environ.* 92 (2009) 377–383.
- [37] W. Gao, M. Wang, C. Ran, X. Yao, H. Yang, J. Liu, D. He, J. Bai, One-pot synthesis of Ag/r-GO/TiO₂ nanocomposites with high solar absorption and enhanced anti-recombination in photocatalytic applications, *Nanoscale* 6 (2014) 5498–5508.
- [38] Q. Niu, X. Gu, L. Li, Y.-n Zhang, G. Zhao, 3D CQDs-{001} TiO₂/Ti photoelectrode with dominant {001} facets: efficient visible-light-driven photoelectrocatalytic oxidation of organic pollutants and mechanism insight, *Appl. Catal. B: Environ.* 261 (2020), 118229.
- [39] L. Ge, C. Han, J. Liu, Novel visible light-induced g-C3N4/Bi2WO₆ composite photocatalysts for efficient degradation of methyl orange, *Appl. Catal. B: Environ.* 108 (2011) 100–107.
- [40] W. Li, C. Zhuang, Y. Li, C. Gao, W. Jiang, Z. Sun, K. Qi, Anchoring ultra-small TiO₂ quantum dots onto ultra-thin and large-sized MXene nanosheets for highly efficient photocatalytic water splitting, *Ceram. Int.* 47 (2021) 21769–21776.
- [41] K. Qi, Y. Xie, R. Wang, S.-y Liu, Z. Zhao, Electroless plating Ni-P cocatalyst decorated g-C3N4 with enhanced photocatalytic water splitting for H₂ generation, *Appl. Surf. Sci.* 466 (2019) 847–853.
- [42] K. Qi, N. Cui, M. Zhang, Y. Ma, G. Wang, Z. Zhao, A. Khataee, Ionic liquid-assisted synthesis of porous boron-doped graphitic carbon nitride for photocatalytic hydrogen production, *Chemosphere* 272 (2021), 129953.
- [43] S. Siahrostami, A. Verdaguera-Casadevall, M. Karimad, D. Deiana, P. Malacrida, B. Wickman, M. Escudero-Escribano, E.A. Paoli, R. Frydendal, T.W. Hansen, I. Chorkendorff, I.E. Stephens, J. Rossmeisl, Enabling direct H₂O₂ production through rational electrocatalyst design, *Nat. Mater.* 12 (2013) 1137–1143.
- [44] J. Masa, W. Xia, M. Muñoz, W. Schuhmann, On the role of metals in nitrogen-doped carbon electrocatalysts for oxygen reduction, *Angew. Chem. Int. Ed.* 54 (2015) 10102–10120.
- [45] Y. Jin, Q. Kang, X. Guo, B. Zhang, D. Shen, G. Zou, Electrochemical-signal-amplification strategy for an electrochemiluminescence immunoassay with g-C3N4 as tags, *Anal. Chem.* 90 (2018) 12930–12936.
- [46] C.P. Mora, F. Martínez, Thermodynamic quantities relative to solution processes of Naproxen in aqueous media at pH 1.2 and 7.4, *Phys. Chem. Liq.* 44 (2006) 585–596.
- [47] Z. Zhang, K. Sun, B. Gao, G. Zhang, X. Liu, Y. Zhao, Adsorption of tetracycline on soil and sediment: effects of pH and the presence of Cu(II), *J. Hazard Mater.* 190 (2011) 856–862.
- [48] L. Liu, G. Zeng, J. Chen, L. Bi, L. Dai, Z. Wen, N-doped porous carbon nanosheets as pH-universal ORR electrocatalyst in various fuel cell devices, *Nano Energy* 49 (2018) 393–402.
- [49] S. Nasseri, A.H. Mahvi, M. Seyedsalehi, K. Yaghmaeian, R. Nabizadeh, M. Alimohammadi, G.H. Safari, Degradation kinetics of tetracycline in aqueous solutions using peroxydisulfite activated by ultrasound irradiation: effect of radical scavenger and water matrix, *J. Mol. Liq.* 241 (2017) 704–714.